American Journal of Energy Engineering
2026, Vol. 14, No. 4, pp. 192–202
https://doi.org/10.11648/j.ajee.20261404.13

SciencePG
Science Publishing Group

Research Article

Diffusion–GAT Dual-Channel Framework for Extreme Few-Shot and Noise-Robust Pump Fault Diagnosis

Wu Heng, Gao Lei, Wang Wenchao*, Zhang Yu, He Biao

State Grid Shaanxi Electric Power Co., Ltd., Xi'an, China

Abstract

Fault diagnosis of main circulation pumps in converter station valve cooling systems is severely challenged by strong electromagnetic interference and extremely limited fault samples. To address these issues, this paper proposes a physics-informed dual-channel collaborative framework that integrates multi-field coupling priors into both data generation and feature learning. First, feature sensitivity and signal correlation matrices are derived from fluid-mechanical-electrical coupling mechanisms to formulate computable physical priors. Second, a physics-informed conditional diffusion model is developed, embedding physical constraints into the reverse denoising process to generate augmented samples consistent with fault evolution laws. Third, a mechanism-initialized graph attention network is constructed with learnable balancing factors that dynamically fuse physical priors with data-driven features. The two channels collaborate implicitly through sensitivity matrices, forming a closed-loop optimization of generation and learning. Experimental results under extreme conditions—only five training samples per class and a signal-to-noise ratio of 5 dB—demonstrate that the proposed method achieves a diagnostic accuracy of 96.8%, outperforming single-channel physics-embedded methods by 6.3 percentage points and purely data-driven methods by 12.2 percentage points. These results validate the effectiveness, robustness, and physical interpretability of the dual-channel collaborative mechanism.

Keywords

HVDC Converter Station, Valve Cooling System, Few-shot Learning, Physics-informed Learning, Diffusion Model, Graph Attention Network

1. Introduction

As a critical hub for AC–DC power conversion, the operational reliability of converter stations directly impacts the security and stability of power grids [1]. The valve cooling system is responsible for heat exchange in converter valves. A failure of the main circulation pump can lead to a loss of temperature control, potentially causing DC blocking or cascading failures [2]. According to State Grid operational statistics from 2018 to 2023, valve cooling system failures accounted for 23% of DC blocking incidents, with main circulation pump failures representing 41% of these events [3, 4]. Consequently, condition monitoring and fault diagnosis of main circulation pumps hold significant engineering value.

Fault evolution in these pumps exhibits strong fluid–mechanical–electrical multi-field coupling. However, early degradation signatures are subtle and often masked by intense

*Correspondence: Wang Wenchao (309210737@qq.com)

Received: 2 September 2026; **Accepted:** 29 September 2026; **Published:** 13 November 2026

Copyright: © The Author(s), 2026. Published by Science Publishing Group. This is an **Open Access** article, distributed under the terms of the Creative Commons Attribution 4.0 License (http://creativecommons.org/licenses/by/4.0/), which permits unrestricted use, distribution and reproduction in any medium, provided the original work is properly cited.

electromagnetic noise from converter valve switching, rendering diagnosis exceptionally challenging [5, 6]. Although deep learning-based intelligent diagnosis has advanced considerably [7, 8], three critical bottlenecks persist under converter station conditions: (i) lack of physical interpretability hinders the embedding of multi-field coupling laws [9-12]; (ii) early fault features are easily misclassified under strong noise [13-15]; and (iii) the extreme scarcity of fault samples induces severe overfitting [16-18]. Physics-informed methods introduce physical priors to constrain the solution space and enhance few-shot generalization [19]. Yet, existing studies largely confine physical embedding to a single stage—either generation or learning—failing to establish effective collaboration between the two, and thus struggle to simultaneously address strong interference and sample scarcity.

Based on the embedding strategy, existing physics-informed approaches fall into three categories: structural constraints (e.g., mechanism-based network topology [20]), loss constraints (e.g., mechanism-derived regularization [21]), and generative constraints (e.g., mechanism-guided data generation [22]). All are limited to isolated stages: structural constraints rely on fixed topologies ill-suited to varying conditions; loss constraints require manual tuning and overlook inter-feature physical correlations; generative constraints do not interact with downstream learning. Critically, no existing work has designed a dual-channel collaborative mechanism tailored to the unique converter station environment (strong electromagnetic interference plus few samples).

To overcome these limitations, this paper proposes a physics-informed dual-channel collaborative framework. The core contributions are:

Dual-channel parallel embedding: Unlike PINN-GNN which applies constraints only at the learning stage, the proposed method embeds physical priors into both the generation process (via a physics-informed conditional diffusion model) and the learning process (via a mechanism-initialized graph attention network), achieving full-process integration of physical knowledge.

Dynamic adaptive fusion: Learnable balancing factors are introduced to dynamically adjust the strength of physical constraints during training, balancing prior reliability and data adaptability.

Mechanism-guided anti-noise design: Physical correlation matrices are used to initialize graph topology priors, enabling the attention mechanism to filter out spurious feature correlations induced by noise.

Under the extreme setting of five training samples per class and an SNR of 5 dB, extensive experiments verify the effectiveness and robustness of the proposed method. Ablation studies and comparative analyses further reveal the collaborative advantages of the dual-channel design over single-channel physical constraints.

2. Fault Mechanism and Multi-Source Signal Characteristics

2.1. Fluid–Mechanical–Electrical Multi-Field Coupling Mechanism

The main circulation pump in a converter station valve cooling system is a strongly coupled fluid–mechanical–electrical system. From an energy-flow perspective, the motor converts electrical energy into mechanical work on the fluid, while fluid kinetic and pressure energy conversion inversely affects rotor dynamics. This section mathematically characterizes three key coupling relationships.

2.1.1. Fluid–Mechanical Coupling

Let the impeller unbalance mass be m_u, eccentricity e, and rotational angular velocity $\Omega_r=n_b f_r$ (where n_b is the number of blades and f_r the rotational frequency). The unbalance centrifugal force is:

$$F_u(t)=m_u e\Omega_r^2\cos(\Omega_r t+\phi_0) \tag{1}$$

where ϕ_0 is the initial phase. This force excites the shaft system, producing rotational frequency components in vibration signals. According to rotor dynamics, the vibration displacement amplitude under unbalance response is:

$$\widehat{X}=\frac{m_u e\Omega_r^2}{k_{eq}\sqrt{(1-\lambda^2)^2+(2\zeta\lambda)^2}} \tag{2}$$

where k_{eq} is the equivalent system stiffness, $\lambda=\Omega_r/\Omega_n$ is the frequency ratio ($\Omega_n=\sqrt{\frac{k_{eq}}{m_{eq}}}$ is the natural frequency), and ζ is the damping ratio. Equation (2) shows that the rotational frequency amplitude varies linearly with unbalance magnitude and nonlinearly with stiffness and damping.

When cavitation occurs, local pressure drops below vapor pressure, causing bubble collapse. The resulting impact pressure p_c can be approximated as:

$$p_c=\frac{1}{2}K\rho v_c^2 \tag{3}$$

where K is an empirical coefficient, \rho is fluid density, and v_c is the bubble collapse velocity. This impact exhibits high-frequency broadband characteristics, with energy concentrated in the 5–20 kHz range.

Bearing wear induces periodic impact pulses due to localized spalling on the rolling contact surface. Consider a defect with circumferential length on the inner raceway; the ball passage frequency over the defect (BPFI) is:

$$f_{BPFI}=\frac{n_b}{2}f_r\left(1+\frac{d_b}{d_p}\cos\alpha\right) \tag{4}$$

where n_b is the number of rolling elements, d_b the ball diameter, d_p the pitch diameter, and the α contact angle. Each time a rolling element strikes the defect, an impact force F_{imp} is generated:

$$F_{imp}(t)=\sum_{m=-\infty}^{+\infty} A_m \delta(t-mT_{BPFI}) \otimes h_{sys}(t) \quad (5)$$

where A_m is the impact amplitude modulated by the load zone, $\delta(\cdot)$the Dirac function, $T_{BPFI}=1/f_{BPFI}$, and h_{sys} the system impulse response. The resulting vibration exhibits high kurtosis (Kurtosis>3.5) due to the impulsive nature of F_{imp}, and the envelope spectrum reveals BPFI and its harmonics, providing the physical basis for the feature mapping in Table 1.

2.1.2. Mechanical-Electrical Coupling

Bearing wear-induced rotor eccentricity alters the air-gap magnetic field. Define eccentricity as $\varepsilon=\delta/g_0$, where δ is the eccentric displacement and g_0 the nominal air-gap length. Under dynamic eccentricity, the air-gap permeance can be expanded as a Fourier series:

$$\Lambda(\theta, t)=\Lambda_0[1+\sum_{n=1}^{\infty} \varepsilon^n \cos n(\theta-\omega_r t)] \quad (6)$$

where Λ_0 is the average air-gap permeance, and the harmonic amplitudes satisfy $\Lambda_n \propto \varepsilon^n$ (with $\varepsilon \ll 1$). The characteristic frequencies in the stator current are then:

$$f_{ecc}=f_s \pm k f_r,\ k=1, 2, 3,\ldots \quad (7)$$

where f_s is the supply fundamental frequency. The sideband amplitude relates to eccentricity as:

$$I_{ecck}=I_0 \cdot \beta_k \cdot \varepsilon \quad (8)$$

with I_0 the fundamental current amplitude and β_k a winding-distribution attenuation factor. For $k=1$, $\beta_1 \approx 1$, indicating high sensitivity of the sideband amplitude to eccentricity and providing a quantitative basis for inferring mechanical faults from current signals.

2.1.3. Fluid-Electrical Coupling

Flow and temperature variations directly affect motor heat dissipation and load characteristics. The stator winding temperature rise ΔT_s is governed by the heat balance:

$$\Delta T_s=\frac{P_{loss}}{\rho c_p Q} \quad (9)$$

where ρ is fluid density, c_p is specific heat capacity, and P_{loss} represents motor losses. A decrease in flow reduces heat dissipation, raises winding temperature, alters stator resistance, and ultimately affects current amplitude and power factor.

2.1.4. Coupling Strength Quantification

To quantify the relative strength of the three-field coupling, a normalized coupling coefficient is defined:

$$\Gamma_{p\,q}=\frac{\mathrm{tr}(F_p^{\top} R_q)}{\|F_p\|_F \|R_q\|_F} \quad (10)$$

where F_p and R_q are the excitation and response feature matrices of physical fields p and q over N sampling instants; tr denotes the trace, and $\|\cdot\|_F$ the Frobenius norm. $\Gamma_{pq}|\to 1$ indicates strong coupling, while $\Gamma_{pq}\approx 0$ indicates weak coupling.

Based on AMESim-Simulink co-simulations with injected typical faults, the computed coupling strengths are: fluid–mechanical $\Gamma_{12}=0.82$, mechanical–electrical $\Gamma_{23}=0.76$, and fluid–electrical direct coupling$\Gamma_{13}=0.31$. This confirms the cascaded "fluid→mechanical→electrical" transmission characteristic and provides a prior weight basis for constructing physical correlation and sensitivity matrices.

2.2. Typical Fault Evolution Laws and Feature Mapping

Table 1 summarizes the evolution laws and multi-source signal feature mapping for four typical fault types, derived from mechanism analysis and engineering measurements. These mappings serve both as diagnostic criteria and as prior knowledge for subsequent physically constrained modeling.

2.3. Multi-Source Signal Physical Correlation Modeling

Based on the above multi-field coupling mechanisms, we

Table 1. Mapping relationships between typical faults and multi-source signal features.

Fault Type	Mechanism Feature	Sensitive Signal	Key Feature Band/Parameter	Feature Extraction Method
Bearing Wear	Contact surface fatigue spalling, impact pulse generation	Vibration, Temperature	High-frequency envelope: BPFI±0.5kHz (inner), BPFO±0.5kHz (outer); Temp trend: >5°C/h	Envelope demodulation (Hilbert), extract BPFI/BPFO sideband amplitude; Kurtosis index (Kurtosis>3.5)

Fault Type	Mechanism Feature	Sensitive Signal	Key Feature Band/Parameter	Feature Extraction Method
Impeller Unbalance	Mass eccentricity causes periodic centrifugal force change	Vibration, Pressure	Rotational frequency: $1f_r$ (dominant), Harmonics: $2f_r$, $3f_r$; Phase stability: <5°	FFT spectrum analysis, extract 1X amplitude and phase, calculate harmonic energy ratio
Cavitation	Local pressure below vapor pressure produces bubble collapse	Pressure, Vibration, Noise	Pressure pulsation: 5-20 kHz broadband; Vibration impact: >10 kHz random; AE: 150-400 kHz	Wavelet packet decomposition (db4, 8 levels), extract 5-20 kHz band energy ratio; AE RMS value
Leakage	Seal failure causes medium loss	Flow, Pressure, Temperature	Flow decrease: >10% rated; Inlet pressure: <-0.05 MPa; Temp difference: > 8℃	Flow integral calculation for flow deviation rate, pressure gradient analysis for pressure drop coefficient

*Table Footnote: The normal state serves as the baseline with no significant feature deviation across all signal channels.

construct a physical correlation matrix $R \in R^{4\times4}$ among the four signal types (vibration, pressure, temperature, flow). The entry R_{ij} represents the expected correlation coefficient between signals i and j under typical faults.

2.3.1. Transfer Function Derivation

Under small perturbations, the pressure pulsation generated by rotating machinery is linearly related to vibration velocity:

$$\Delta P_{puls}(t)=K_{fv}\cdot\Delta v_{vib}(t) \tag{11}$$

where $K_{fv}=\rho A_{blade}\omega_r/A_{duct}$ is the fluid–structure coupling coefficient. For temperature–flow correlation, differentiating the energy conservation equation $P_{loss}=\rho c_p Q\Delta T_w$ yields:

$$\frac{d(\Delta T_w)}{dQ}=-\frac{P_{loss}}{\rho c_p Q^2} \tag{12}$$

indicating a negative correlation with sensitivity inversely proportional to flow squared.

2.3.2 Feature Sensitivity Analysis

The sensitivity of feature i to fault class k is defined as the relative rate of change of the power spectral density within the sensitive frequency band $[\omega_L,\omega_H]$ (from Table 1):

$$S_{ik}=\int_{\omega_L}^{\omega_H}\left|\frac{\partial \ln P_{x_i}(\omega;\theta_k)}{\partial\theta_k}\right|_{\theta_{k,0}} d\omega \tag{13}$$

where $P_{x_i}(\omega;\theta_k)$ is the parameterized PSD estimate and $\theta_{k,0}$ the baseline normal-state parameter. The logarithmic derivative form eliminates dimensional effects.

The mechanism-driven sensitivity matrix S^{mech} is computed via physical field transfer:

$$S^{mech}=Y\cdot\Gamma\cdot\Omega\in R^{N_f\times K} \tag{14}$$

where Y, Γ, and Ω represent signal–field mapping, inter-field coupling, and field–fault correlation, respectively. The data-driven component S^{data} is obtained from normalized mutual information on source domain data. The final sensitivity matrix is fused using mechanism confidence weights α_k:

$$S_{i,k}=\alpha_k\cdot S_{i,k}^{mech}+(1-\alpha_k)\cdot S_{i,k}^{data} \tag{15}$$

with $\alpha_k=0.7$ for well-understood faults (bearing wear, unbalance), 0.5 for moderately complex (cavitation), and 0.4 for strongly nonlinear (Leakage). A lower bound $\eta_{min}=0.3$ is enforced for features marked as sensitive in Table 1.

2.3.3. Simulation Calibration and Experimental Validation

Using an AMESim-Simulink co-simulation platform, a pump–pipe–valve model was built and various faults injected. The simulated physical correlation matrix R_{sim} was obtained via Pearson correlation. After laboratory validation, the lower bound of the 95% confidence interval is adopted as a conservative estimate:

$$R_{final}=R_{sim}-1.96\sigma_R \tag{16}$$

where σ_R is the standard deviation matrix from repeated experiments. For brevity, R_{final} is denoted as R hereafter. Main symbols are listed in Table 2.

Table 2. Main index symbols.

Symbol	Dimension/Range	Meaning
I	1<=i<=d	Feature dimension index
K	1<=k<=K	Fault category index (K=5)
S	{vib, pre, temp, flow}	Signal type index
P	{fluid, mech, elec}	Physical field index
Γ	$R^{3\times3}$	Inter-field coupling strength matrix
Ω	$R^{3\times K}$	Physical field-fault coupling matrix
Y	$R^{N_f\times3}$	Signal-physical field coupling matrix
S	$R^{N_f\times K}$	Feature sensitivity matrix
R	$R^{4\times4}$	Inter-signal physical correlation matrix
C	$R^{93\times1}$	Physical constraint vector

3. Physics-Informed Dual-Channel Framework for Multi-Source Signal Fusion

3.1. Overall Framework

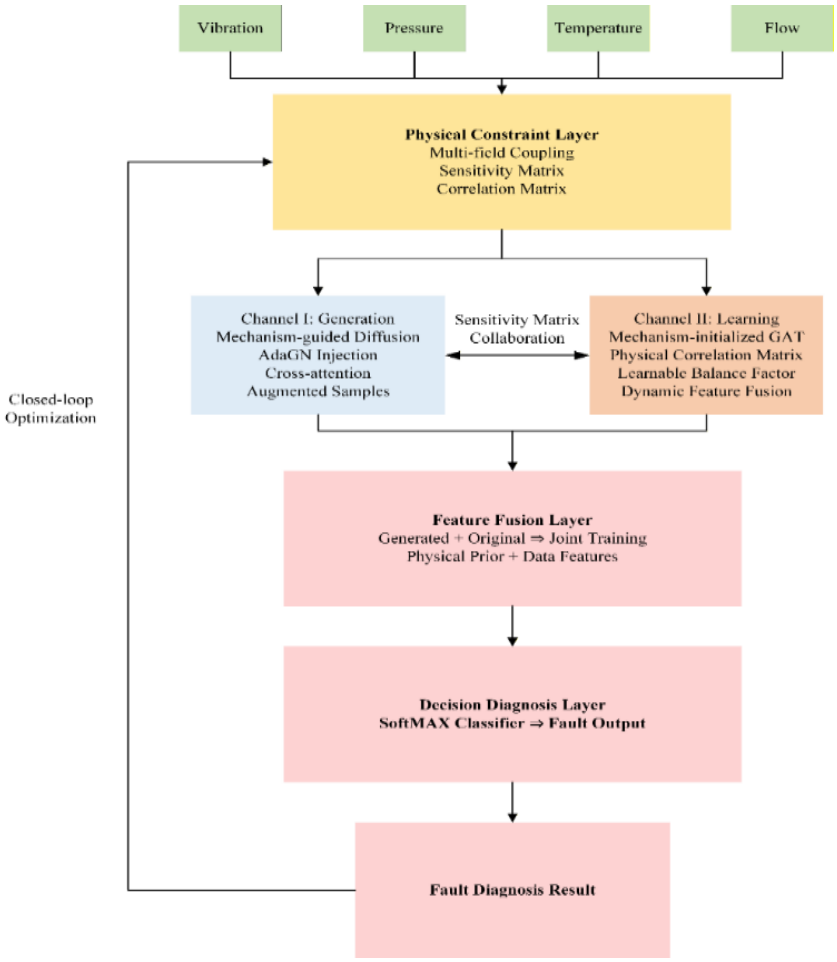


Figure 1. Overall framework of the proposed method. (GAT: Graph Attention Network).

The proposed framework, illustrated in Figure 1, comprises four layers: physical constraint, data augmentation, feature fusion, and decision diagnosis. The core idea is dual-channel parallel embedding:

Channel I (Generation Augmentation): Physical constraints are injected into the data generation process via a physics-informed conditional diffusion model.

Channel II (Learning Optimization): Physical correlation matrices serve as initialization priors for a graph attention network (GAT).

The two channels collaborate implicitly through the sensitivity matrix S: Channel I uses S to construct conditional vectors guiding sample generation, while Channel II uses S to formulate a consistency loss that constrains feature attention. The feature fusion layer initializes the GAT adjacency matrix with R and employs learnable balancing factors to fuse physical priors with data-driven features. The decision layer outputs the fault category.

3.2. Physical Constraint Modeling and Feature Correlation Rules

Define the fault feature vector $X=[x_{vib},x_{pre},x_{temp},x_{flow}]^T$ and the label matrix \mathb $Y\in[0,1]^{N\times K}$. The source domain consists of laboratory-simulated fault data (200 groups per class, covering mild/moderate/severe levels) under operating conditions of 2400–3200 r/min and 120–200 m^3/h.

3.2.1. Sensitivity Matrix Derivation

The mechanism-driven sensitivity is computed via (14), and the data-driven component via normalized mutual information (17):

$$S_{i,k}^{data}=\frac{I(x_i;y_k)}{H(x_i)}\in[0,1] \tag{17}$$

3.2.2. Correlation Matrix and Adaptive Fusion

The physical prior correlation is initialized from transfer functions and refined using distance correlation (dCor) to capture nonlinear dependencies:

$$dCor(X,Y)=\frac{dCov(X,Y)}{\sqrt{dVar(X)\cdot dVar(Y)}} \tag{18}$$

A bias-corrected estimator is used for small samples. The final estimated correlation is fused via an adaptive balancing factor \gamma (0.8 for clear correlations, 0.5 for complex ones):

$$r_{st}^{est}=\gamma\cdot r_{st}^{mech}+(1-\gamma)\cdot r_{st}^{post} \tag{19}$$

where γ is set according to physical cognition reliability: $\gamma=0.8$ for clear mechanism correlations (vibration-pressure), $\gamma=0.5$ for complex mechanism correlations (temperature-pressure).

To accommodate varying operating conditions, an adaptive expected correlation degree is updated per epoch:

$$\hat{R}_{s,t}^{[l]}=\sigma(\eta^{[l]})\cdot\tilde{R}_{s,t}+(1-\sigma(\eta^{[l]}))\cdot\hat{R}_{s,t}^{[l-1]} \tag{20}$$

where $\hat{R}_{s,t}^{[l]}$ is a learnable balancing factor, σ denotes the sigmoid function. The mechanism consistency loss is:

$$L_{mc}=\frac{1}{2}\sum_{i=1}^{S}\sum_{j=1}^{S}\left\|R_{ij}-\hat{R}_{ij}^{(l)}\right\|_2^2 \tag{21}$$

Additionally, a feature sensitivity consistency constraint is introduced:

$$L_{sen}=\sum_{i=1}^{N_f}\left\|\nabla_{x_i}L_y-g_i\right\|_2^2 \tag{22}$$

where $\nabla_{x_i}L_y$ is the gradient of classification loss to feature i, and $g_i=S_{i,y}\cdot\left\|\nabla_x L_y\right\|/\left\|S_{:,y}\right\|$ is mechanism expected gradient.

3.3. Physics-Informed Conditional Diffusion Model

3.3.1. Physical Constraint Vector Construction

The physical constraint vector $c\in R^{93}$ concatenates four encodings:

Sensitivity encoding $c_{sens}\in R^{16}$: Based on sensitivity matrix, mapped through a Multi-Layer Perceptron (MLP) ($N_f\to32\to16$, ReLU activation);

Correlation encoding $c_{corr}\in R^{24}$: Based on upper triangle of physical correlation matrix $R_{upper}\in R^{10}$, mapped through MLP($10\to48\to24$);

Operating condition encoding $c_{cond}\in R^{44}$: Including normalized values of flow, temperature, pressure, rotational speed $x_{oper}\in R^4$ and frequency domain mask $m_{freq}\in R^{40}$ based on sensitive frequency bands in Table 1;

Coupling encoding $c_{coupling}\in R^9$: Based on vectorized physical field coupling matrix $\Gamma\in R^{3\times3}$, mapped through MLP($9\to18\to9$).

Finally:

$$c=[c_{sens}^T,c_{corr}^T,c_{cond}^T,c_{coupling}^T]^T\in R^{93} \tag{23}$$

3.3.2. Condition Injection via AdaGN and Cross-Attention

Condition injection employs Adaptive Group Normalization (AdaGN) with a 2-layer MLP mapping network (hidden dim 256):

$$h_{map}=ReLU(W_1c+b_1)\in R^{256}$$

$$\gamma_{ada}=W_\gamma h_{map}+b_\gamma,\beta_{ada}=W_\beta h_{map}+b_\beta \quad (24)$$

AdaGN operation is defined as:

$$AdaGN(h, c)_{:,i}=\gamma_{ada,i}(c)\cdot\frac{h_{:,i}-\mu_i}{\sqrt{\sigma_i^2+\epsilon}}+\beta_{ada,i}(c) \quad (25)$$

where $h\in R^{N\times d_h}$ is intermediate feature map; GroupNorm statistics are $\mu_i=\frac{1}{N}\sum_{j=1}^{N}h_{j,i}$, $\sigma_i^2=\frac{1}{N}\sum_{j=1}^{N}(h_{j,i}-\mu_i)^2$; $\epsilon=10^{-6}$ is numerical stability constant.

A cross-attention mechanism further enables the decoder to focus on encoder features guided by c:

$$CrossAttn(E, c)=softmax\left(\frac{QK^T}{\sqrt{d_k}}\right)V \quad (26)$$

where $Q=EW_Q$, and K,V are derived from c.

3.3.3. Training Objective

The forward diffusion process is defined as:

$$q(x_t|x_{t-1})=N(x_t;\sqrt{1-\beta_t}x_{t-1},\beta_t I)$$

$$q(x_t|x_0)=N(x_t;\sqrt{\bar{\alpha}_t}x_0,(1-\bar{\alpha}_t)\,I) \quad (27)$$

The reverse process predicts the noise $\boldsymbol{\epsilon}_\theta(\mathbf{x}_t,t,\mathbf{c})$. The training objective is the simplified variational bound:

$$L_{diff}=E_{t\sim U\{1,\ldots,T\},x_0\sim q(x_0),\epsilon\sim N(0,I)}\left[//\epsilon-\epsilon_\theta(x_t,t,c)//_2^2\right] \quad (28)$$

3.4. Mechanism–Data Collaborative Diagnosis Network

3.4.1. Physics-Initialized Graph Attention Fusion

Multi-source features are treated as graph nodes. The initial adjacency matrix is directly initialized from the physical correlation matrix R:

$$A_{ij}^{(0)}=\begin{cases}R_{s(i),s(j)} & \text{If features i and j belong to the same signal type}\\ \kappa\cdot R_{s(i),s(j)} & \text{If features i and j are from distinct signal types}\end{cases} \quad (29)$$

where $\kappa=0.5$ is the cross-signal scaling factor. During training, attention coefficients are dynamically fused:

$$\alpha_{s\to t}^{(l)}=(1-\sigma(\eta^{(l)}))\cdot\alpha_{s\to t}^{(l),data}+\sigma(\eta^{(l)})\cdot\alpha_{s\to t}^{(l),mech} \quad (30)$$

Message passing process is:

$$h_s^{(l+1)}=ReLU\left(\sum_{t\in N_s}\alpha_{st}^{(l)}W^{(l)}h_t^{(l)}\right) \quad (31)$$

A 3-layer GAT with 8 attention heads per layer (hidden dim 128, output dim 64) is employed, with residual connections, dropout, and layer normalization.

3.4.2. Total Loss Function

The total loss combines classification, physical consistency, and regularization terms:

$$L_{total}=L_{CE}+\mu_1L_{mc}+\mu_2L_{sen}+\mu_3L_{reg} \quad (32)$$

where $L_{reg}=//\theta//_2^2$. Hyperparameters $\mu_1=0.1$, $\mu_2=0.05$, $\mu_3=0.01$ were determined via five-fold cross-validated grid search over $\{0.001, 0.005, 0.01, 0.05, 0.1, 0.5\}$.

4. Experimental Verification and Results Analysis

4.1. Experimental Platform and Dataset

Experiments were conducted on a converter station valve cooling system simulation platform. The main circulation pump has a rated power of 45 kW, rated flow of 180 m^3/h, rated head of 45 m, and rated speed of 2900 r/min. Five states were considered: normal, bearing wear, impeller unbalance, cavitation, and leakage, each with mild, moderate, and severe levels. Sensors include triaxial accelerometers, pressure transducers, temperature sensors, and flowmeters.

The source domain comprises 200 laboratory-simulated samples per class (covering three severity levels) under 2400–3200 r/min and 120–200 m^3/h. It serves exclusively for pre-training the physics-informed conditional diffusion model and constructing the physical prior matrices S and R, and is not used in the few-shot classifier training stage. The target domain consists of 160 independent field-simulated samples per class acquired from the same platform under identical operating conditions, simulating realistic on-site few-shot scenarios. For each fault class, 5, 10, and 20 samples were randomly drawn as training sets via stratified sampling across severity levels (mild/moderate/severe), yielding remaining test sets of 155, 150, and 140 samples per class, respectively. The pre-trained diffusion model subsequently generates 100 augmented samples per class conditioned on the target-domain

fault labels and operating parameters; these generated samples are concatenated with the few-shot real training samples to form the final augmented training set for the GAT classifier. Each experimental setting was repeated 10 times with different random seeds; results are reported as mean accuracy ± standard deviation.

Ablation Protocol. Five variants are designed under the 5-shot setting with identical data splits: (i) Full Model: complete framework with physics-informed diffusion + GAT; (ii) w/o Generation: diffusion disabled, GAT trained on 5 real samples with physical priors; (iii) w/o Learning: GAT replaced by MLP, diffusion with physical priors retained; (iv) w/o Physics Embedding: all physical constraints disabled (R=I, S uniform) and diffusion disabled, equivalent to a purely data-driven baseline; (v) w/o Source-Domain Data: no source-domain data used, trained from scratch on 5-shot target samples.

4.2. Comparative Results

Six categories of methods were compared: (1) Single-source CNN (1D ResNet-18); (2) Multi-source fusion CNN (early concatenation); (3) Multi-source GNN without constraints; (4) PINN-GNN [23]; (5) Meta-learning (MLIIO) [24]; (6) Standard diffusion model (DDPM) [25]. An ablation variant "Proposed (No Diffusion)" is also included.

Key observations:

1) Multi-source fusion improves accuracy by over 12 percentage points over single-source CNN, confirming the value of multi-sensor complementarity.
2) Physics-informed methods (PINN-GNN, proposed) consistently outperform purely data-driven approaches, highlighting the importance of physical priors.
3) The proposed dual-channel framework surpasses the best competitor (DDPM) by 3.4 percentage points and PINN-GNN by 6.3 percentage points under the 5-sample setting, demonstrating the collaborative advantage of dual-channel physics embedding.

Table 3. *Diagnostic performance under few-shot conditions (Mean ± Std).*

Method	Feature Extractor	Fusion Strategy	5 samples/class	10 samples/class
Single-source CNN	ResNet-18	-	72.3±3.2%	78.5±2.1%
Multi-source Fusion CNN	ResNet-18	Early Concat	84.6±2.8%	88.3±1.9%
Multi-source GNN (No Constraint)	ResNet-18	GAT (No Constraint)	88.2±2.1%	91.7±1.5%
PINN-GNN	ResNet-18	Physical Loss GNN	90.5±1.8%	93.2±1.3%
MLIIO	ResNet-18	Intra/Inter-class Opt	92.1±1.5%	94.6±1.1%
DDPM	ResNet-18	Traditional Diffusion	93.4±1.4%	95.3±1.0%
Proposed w/o Generation Channel	ResNet-18	GAT with Physical Prior	89.5±2.0%	92.4±1.4%
Proposed (Dual-Channel)	ResNet-18	Physics-Informed Diffusion + GAT	96.8±1.2%	97.5±0.9%

*Table Footnote: All methods share the same source-domain data for feature extractor pre-training. “Proposed w/o Generation” and “Proposed (Dual-Channel)” correspond to ablation variants in Table 4.

A paired t-test between the proposed method and DDPM under 5 samples/class yields $t = 8.73$, $p < 0.001$, and Cohen's $d > 0.8$, confirming statistical significance with a large effect size [26].

Noise Robustness: As shown in Figure 2, under 5 dB SNR the proposed method achieves 84.8% accuracy, outperforming PINN-GNN (79.3%) and DDPM (76.5%) by 5.5 and 8.3 percentage points, respectively. This robustness stems from (i) physical constraints focusing attention on sensitive frequency bands, and (ii) graph attention filtering spurious noise-induced correlations.

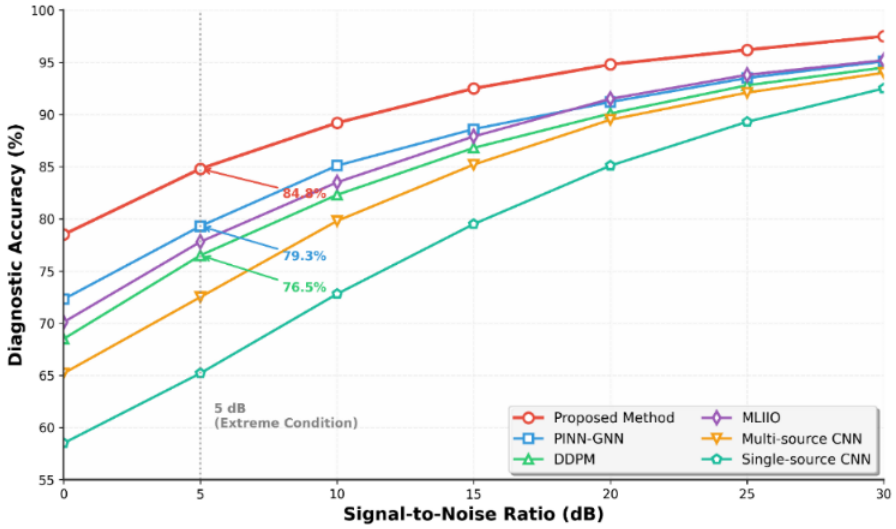


Figure 2. Diagnostic accuracy comparison under different SNR conditions (5 samples per class).

4.3. Computational Complexity and Generated Sample Quality

The main computational load arises from the T-step denoising, GAT message passing, and physical constraint evaluation. On an NVIDIA RTX 3090 GPU, single-sample inference takes ~45 ms, meeting online monitoring requirements (<100 ms). Pre-training the diffusion model eliminates the need for online iterative physical equation solving, yielding approximately a threefold speedup over PINN-GNN [27].

Generated sample quality was assessed via:

Physical consistency: Key frequency band energy deviation is 3.2% (vs. 8.7% for DDPM); signal correlation deviation is 0.08 (vs. 0.23); fault evolution rationality score is 92.5% (vs. 76.3%).

Classification effectiveness: With up to 60% generated samples, the proposed method maintains >95% accuracy, whereas DDPM accuracy drops below 90% when generated samples exceed 40%.

4.4. Ablation Study

Table 4. Module ablation results (5 samples/class).

Configuration	Accuracy	Δ vs. Full	Physics Embedding	Diffusion	GAT
Full Model	96.8%	—	Gen. + Learn.	✓	✓
w/o Generation	89.5%	–7.3%	Learning only	✗	✓
w/o Learning	91.2%	–5.6%	Generation only	✓	✗ (MLP)
PINN-GNN	90.5%	–6.3%	Loss only	✗	✓
w/o Physics Embedding	84.6%	–12.2%	None	✗	✓ (no prior)
w/o Source-Domain Data	83.4%	–13.4%	None	✗	✓ (no prior)

*Table Footnote: "w/o Physics Embedding" disables all physical priors and does not employ diffusion augmentation; it coincides with the purely data-driven "Multi-source Fusion CNN" baseline in Table 3. The 1.2% gap between "w/o Physics Embedding" and "w/o Source-Domain Data" indicates that source-domain pre-training alone yields marginal improvement without physics embedding.

The two channels exhibit a near-additive contribution pattern: individual removals cause 7.3% and 5.6% drops, respectively, while complete physics disabling causes 12.2%—quantitatively close to the sum (12.9%). The 0.7% gap indicates weak overlap; the generation channel enforces consistency in the sample space, while the learning channel enforces consistency in the feature space, covering complementary physical aspects.

5. Conclusion

This paper has presented a physics-informed dual-channel collaborative framework for diagnosing main circulation pump faults in converter station valve cooling systems under the dual challenges of strong electromagnetic interference and scarce fault samples. By embedding multi-field coupling physical priors in parallel into both a conditional diffusion model (generation channel) and a graph attention network (learning channel), the framework achieves closed-loop optimization where generation respects physical laws and learning adheres to physical constraints. Experimental results under extreme conditions (5 samples/class, 5 dB SNR) demonstrate a diagnostic accuracy of 96.8%, outperforming single-channel physics-embedded methods by 6.3 percentage points and pure data-driven methods by 12.2 percentage points. These findings validate the significant advantages and physical interpretability of the dual-channel collaborative mechanism. Future work will focus on online physical constraint updating, lightweight network design, and cross-station transfer learning to facilitate full-lifecycle optimization and practical engineering deployment.

Abbreviations

AC	Alternating Current
DC	Direct Current
PINN	Physics-Informed Neural Network
GNN	Graph Neural Network
SNR	Signal-to-Noise Ratio
BPFI	Ball Pass Frequency, Inner Race
AMESim	Advanced Modeling Environment for Performing Simulation of Engineering Systems
PSD	Power Spectral Density
GAT	Graph Attention Network
MLP	Multi-Layer Perceptron
AdaGN	Adaptive Group Normalization
CNN	Convolutional Neural Network
DDPM	Denoising Diffusion Probabilistic Model

Author Contributions

Wu Heng: Conceptualization, Resources
Gao Lei: Project administration, Writing – original draft
Wang Wenchao: Data curation, Software
Zhang Yu: Writing – review & editing
He Biao: Investigation

Funding

This work was supported by the Science and Technology Project of State Grid Shaanxi Electric Power Co., Ltd.

Data Availability Statement

The data is available from the corresponding author upon reasonable request.

Conflicts of Interest

The authors declare no conflicts of interest.

References

[1] Ding C, Zheng S, He J, et al. Abnormal detection method for main pump in nuclear power plant based on dynamic multivariate state estimation. *Science Technology and Engineering*, 2025, 25(27): 1–8. (in Chinese).

[2] Zhang Y, Huang Q, Xu W, et al. Progress and challenges of soft measurement technology in pump fault diagnosis in nuclear power plants. *Nuclear Engineering Research and Design*, 2026, 38(2): 45–52. (in Chinese).

[3] Zhao Z, Gao H, Teng M, et al. Fault cause analysis and hidden danger treatment of main circulation pump in valve cooling system of VSC-HVDC converter station. *Hunan Electric Power*, 2025, 45(03): 89–94. (in Chinese).

[4] Liu Y, Yang R, Zheng L, et al. Review on condition monitoring and intelligent operation and maintenance of valve hall in UHV converter station. *High Voltage Engineering*, 2025, 51(08): 4285–4299. (in Chinese).

[5] Meng Z, Chen L, Chen Y, et al. Fault diagnosis method for pump room equipment based on multi-point voltage and current information fusion. *Journal of Hunan University (Natural Sciences)*, 2024, 51(10): 123–131. (in Chinese).

[6] Tang S N, Jiang Y X, Su H, et al. A fault identification method of hydraulic pump fusing long short-term memory and synchronous compression wavelet transform. *Applied Acoustics*, 2025, 201: 109234.

[7] Zaman W, Ahmad Z, Kim J M. Fault diagnosis in centrifugal pumps: A dual-scalogram approach with convolution autoencoder and artificial neural network. *Sensors*, 2024, 24(8): 2456.

[8] Jiang R, Yuan Z, Wang H, et al. Intelligent fault diagnosis of hydraulic systems based on multisensor fusion and deep learning. *IEEE Transactions on Instrumentation and Measurement*, 2024, 73: 3526515.

[9] Silva L H P D, Rodrigues A, Varejao F, et al. Electrical submersible pump fault diagnosis based on 2D transformation of vibration signals and transfer learning of image classification networks. *Neural Computing and Applications*, 2025, 37(12): 8976–8992.

[10] Kong Y, Zhang J, Lu Y, et al. Intelligent fault diagnosis method for equipment system based on data fusion and enhanced graph convolution. *Acta Armamentarii*, 2025, 46(12): 2890–2900.

[11] Zhou Y, Gao L, Guo H, et al. Fault diagnosis of marine screw pump based on multi-sensor information fusion. *Chinese Journal of Ship Research*, 2025, 20(6): 178–186.

[12] Tong X, Yang P, Zhao J. Hybrid fault diagnosis method for gearbox based on data fusion. *Mechanical Engineering & Automation*, 2024(5): 189–192.

[13] Liu Y, Chen S, Cong Z, et al. Key technologies and application prospects of digital twin in power equipment industry. *High Voltage Engineering*, 2021, 47(05): 1539–1554.

[14] Du B, Zhong F, Hou Q, et al. Key scientific issues, challenges and prospects of large models for power systems. *Proceedings of the CSEE*, 2026.

[15] Zhou N, Liao J, Wang Q, et al. Analysis and prospect of deep learning application in smart grid. *Automation of Electric Power Systems*, 2019, 43(04): 180–191.

[16] Lu S, Chao Q, Liu C. Abnormal detection method for plunger pump based on multi-channel vibration information fusion. *Chinese Hydraulics & Pneumatics*, 2023(7): 134–140.

[17] Yu L. Transfer fault diagnosis method for rotating machinery based on multi-source information fusion. Xi'an: Xidian University, 2023: 1–60.

[18] Gultekin O, Cinar E. Deep meta-learning-based multi-signal data fusion approach for fault diagnosis. *Journal of Intelligent Manufacturing*, 2025, 36(3): 789–805.

[19] Liu S, Yin J, Hao M, et al. Fault diagnosis study of hydraulic pump based on improved symplectic geometry reconstruction data enhancement method. *Advanced Engineering Informatics*, 2024, 59: 102134.

[20] Gong F, Tong S, Du C, et al. A fault diagnosis model of an electric submersible pump based on mechanism knowledge. *Sensors*, 2025, 25(11): 5678.

[21] Guo J, Gu F, Ball A. Multivariate fusion covariance matrix network and its application in multichannel fault diagnosis with fewer training samples. *IEEE Transactions on Cybernetics*, 2024, 54(5): 2876–2887.

[22] Chen D, Zhou F, Wang Q. Fusion fault diagnosis method based on multi-source heterogeneous information transfer learning. *Journal of Information Engineering University*, 2020, 21(2): 153–158.

[23] Tao F, Li Y, Wei Y, et al. Data-model fusion method for intelligent manufacturing and digital engineering. *Engineering*, 2025, 55(12): 36–50.

[24] Lai Z, Luo L, Xu D, et al. Cross-domain few-shot fault diagnosis based on diffusion model. *Journal of Vibration and Shock*, 2025, 44(18): 273–283.

[25] Yang X, Ye T, Yuan X, et al. A novel data augmentation method based on denoising diffusion probabilistic model for fault diagnosis under imbalanced data. *IEEE Transactions on Industrial Informatics*, 2024, 20(5): 7820–7831.

[26] Cohen J. *Statistical Power Analysis for the Behavioral Sciences*. 2nd ed. Hillsdale, NJ: Lawrence Erlbaum Associates, 1988: 20–27.

[27] Lai C, Ahmed I, Zio E, et al. A multistage physics-informed neural network for fault detection in regulating valves of nuclear power plants. *Energies*, 2024, 17(11): 2647.